A Theory for Mixed Vortex Rossby–Gravity Waves in Tropical Cyclones

WEI ZHONG

Nanjing Institute of Mesoscale Meteorology, and Key Laboratory of Meteorological Disaster of the Ministry of Education, Nanjing University of Information Science and Technology, Nanjing, China

DA-LIN ZHANG

Department of Atmospheric and Oceanic Science, University of Maryland, College Park, College Park, Maryland, and Key Laboratory of Meteorological Disaster of the Ministry of Education, Nanjing University of Information Science and Technology, Nanjing, China

HAN-CHENG LU

Nanjing Institute of Mesoscale Meteorology, Nanjing, China

(Manuscript received 5 January 2009, in final form 23 July 2009)

ABSTRACT

Vortex–Rossby waves (VRWs) and inertial gravity waves (IGWs) have been proposed to explain the propagation of spiral rainbands and the development of dynamical instability in tropical cyclones (TCs). In this study, a theory for mixed vortex–Rossby–inertia–gravity waves (VRIGWs), together with VRWs and IGWs, is developed by including both rotational and divergent flows in a shallow-water equations model. A cloud-resolving TC simulation is used to help simplify the radial structure equation for linearized perturbations and then transform it to a Bessel equation with constant coefficients. A cubic frequency equation describing the three groups of allowable (radially discrete) waves is eventually obtained. It is shown that low-frequency VRWs and high-frequency IGWs may coexist, but with separable dispersion characteristics, in the eye and outer regions of TCs, whereas mixed VRIGWs with inseparable dispersion and wave instability properties tend to occur in the eyewall. The mixed-wave instability, with shorter waves growing faster than longer waves, appears to explain the generation of polygonal eyewalls and multiple vortices with intense rotation and divergence in TCs. Results show that high-frequency IGWs would propagate at half their typical speeds in the inner regions with more radial ''standing'' structures. Moreover, all the propagating waves appear in the forms of spiral bands with different intensities as their radial widths shrink in time, suggesting that some spiral rainbands in TCs may result from the radial differential displacements of azimuthally propagating perturbations.

1. Introduction

The tropical cyclone (TC) can be viewed as a self-sustaining, axisymmetric vortex with a life span of several days. Superposed on the vortex are often spiral rainbands, polygonal or double eyewalls with variable distribution of cumulus convection, and convectively generated vortices (Schubert et al. 1999; Kossin et al. 2002; Gall et al. 1998). Because of the short life cycle of deep convection, these asymmetric elements interacting with large-scale flows and inner-core dynamics can lead to significant changes in the structure and intensity of TCs on a time scale of hours (Tuleya and Kurihara 1981; Bender 1997; Liu et al. 1997, 1999). Thus, numerous theoretical, observational, and modeling studies have been conducted during the past decades to examine how the asymmetrical features form and then evolve together with the quasi-balanced TC vortices. Earlier studies attribute the development of spiral rainbands to the outward propagation of internal inertia–gravity waves (IGWs; e.g., Willoughby 1978; Xu 1983). However, radar observations indicate that internal IGWs often propagate at speeds that are much faster than those of spiral rainbands. Thus, more research interest has shifted since the 1990s to the vortex–Rossby wave

Corresponding author address: Dr. Da-Lin Zhang, Department of Atmospheric and Oceanic Science, University of Maryland, College Park, MD 20742–2425.
E-mail: dalin@atmos.umd.edu

DOI: 10.1175/2009JAS3060.1

(VRW) theory of MacDonald (1968), who drew an analogy between the movement of spiral rainbands and the propagation of Rossby waves around a rotating planet.

Guinn and Schubert (1993) hypothesized that during the intensifying stage the potential vorticity (PV) field might become more circular, with its highest values at the TC center, and then the radial PV gradient would provide a basic state on which VRWs can propagate. By invoking an analogy between radial gradients of the basic-state absolute vorticity in TCs and meridional gradients of the planetary vorticity in large-scale weather systems, Montgomery and Kallenbach (1997, hereafter MK97) advanced the VRW theory by obtaining the following local dispersion relation of radially and azimuthally propagating VRWs near the radius of $r = r_0$ from the nondivergent barotropic vorticity equation:

$$\omega_R = n\overline{\Omega}_0 + \frac{n\, d\,\overline{\eta}_0/dr}{r_0(k^2 + n^2/r_0^2)}, \tag{1}$$

where $\overline{\Omega}_0$ and $d\,\overline{\eta}_0/dr$ are the mean angular velocity and the mean radial absolute vorticity gradient at a given radius $r = r_0$, respectively, and k and n are the radial and azimuthal wavenumber (WN), respectively. Because its phase velocity is close to that of spiral rainbands, the VRW theory has widely been used to explain the structural changes and the formation of spiral rainbands (e.g., Montgomery and Enagonio 1998; Schubert et al. 1999; Montgomery and Franklin 1998; Wang 2002; Montgomery et al. 2006) and double eyewalls in TCs (Hogsett and Zhang 2009).

Apparently, the IGW and VRW theories, describing the respective divergent and rotational flows, have their own deficiencies in providing a more complete understanding of TC dynamics. Recent observational and high-resolution modeling studies of TCs show the coexistence of strong divergence and rotation in the eyewall (Jorgensen 1984; Liu et al. 1999; Frank and Ritchie 1999). This implies that the TC wave dynamics would not be complete without simultaneously incorporating the effects of rotational and divergent motions, and that both IGWs and VRWs would likely play important roles in TC wave dynamics. Shapiro and Montgomery (1993) pointed out that because of the rapid rotation, there is no clear separation in time scales between the "fast" IGWs and "slow" VRWs in the hurricane core regions. However, Chen et al. (2003) were able to separate IGWs from VRWs in a simulated hurricane using an empirical normal mode method. On the other hand, Ford (1994) found that high azimuthal WN instability in Rankine-like vortices is of the mixed type of VRWs and IGWs. Schecter and Montgomery (2004, hereafter SM04) have also studied the instability of VRWs and showed that VRWs can excite outward-propagating IGWs outside the critical layer when the Rossby number is greater than unity.

The mixed-wave concept implied above refers to the coexistence of two or more different types of waves in a dynamical system. In fact, the atmospheric flows at any instant may consist of many types of wave motions at different scales because of the presence of compressibility, gravity (g), earth rotation (f), and curvature (β) (Holton 2004). But most mixed waves are simply linear superimposition of their associated eigenfrequencies because their restoring forces can be clearly separated. A good example is the mixed IGWs, which could degenerate to pure gravity and inertia waves when one of the restoring forces becomes negligible. Another type of mixed waves is inseparable waves, such as the equatorial Rossby–gravity waves containing both divergence and rotation (Matsuno 1966). This is because the mixed Rossby–gravity waves will no longer exist if either the earth curvature (β) or gravitational effect (g) is neglected. So far, few studies have been conducted to examine if there is any inseparable mixed wave in TCs.

In this study, we attempt to show the existence of an inseparable class of mixed vortex–Rossby–inertia–gravity waves (VRIGWs) that possess both rotation and divergence in TCs. This will be explored by using a rotating shallow-water equations model in the cylindrical coordinates. The next section describes the theoretical framework used to study these waves in relation to the VRW theory of MK97. Section 3 shows derivation of three groups of normal-mode solutions for azimuthally propagating IGWs, VRWs, and mixed VRIGWs after some simplifications based on a cloud-resolving simulation of Hurricane Andrew (1992). Section 4 presents stability analyses and the regions favoring the development of the three different waves and then shows their associated propagating characteristics. A summary and concluding remarks are given in the final section.

2. Theoretical framework

Because of the dominant axisymmetrical structure of TCs, we start from the simplest linearized, f-plane, shallow-water equations in polar (r, λ) coordinates:

$$\left(\frac{\partial}{\partial t} + \overline{\Omega}\frac{\partial}{\partial \lambda}\right)u' - \left(\overline{\eta} - r\frac{d\overline{\Omega}}{dr}\right)v' + g\frac{\partial h'}{\partial r} = 0, \tag{2a}$$

$$\left(\frac{\partial}{\partial t} + \overline{\Omega}\frac{\partial}{\partial \lambda}\right)v' + \overline{\eta}u' + g\frac{\partial h'}{r\partial \lambda} = 0, \tag{2b}$$

$$\left(\frac{\partial}{\partial t} + \overline{\Omega}\frac{\partial}{\partial \lambda}\right)h' + HD' + \kappa u'\frac{dH}{dr} = 0, \tag{2c}$$

where u' and v' are the radial and tangential perturbation velocity, respectively; h' and H are the perturbation height and equivalent mean depth, respectively; $\overline{\Omega}(r) = \overline{V}(r)/r$ is the mean angular velocity, where $\overline{V}(r)$ is the mean tangential wind; $\overline{\eta} = f + 2\overline{\Omega} + rd\overline{\Omega}/dr$ is the mean absolute vorticity; $D' = \partial ru'/r\partial r + \partial v'/r\partial\lambda$ denotes the perturbation divergence; and the parameter κ, set to either 1 or 0, is used herein to trace the effect of the radial advection of the mean height by perturbation flows. We assume that the basic state is in gradient wind balance; that is,

$$f\overline{V} + \frac{\overline{V}^2}{r} = g\frac{dH}{dr}.$$

A concise linearized form of Eq. (2), including both the rotational and divergent components of wave motions, is the shallow-water PV conservation equation,

$$\frac{d}{dt}\left(\frac{\overline{\eta} + \zeta'}{H + h'}\right) = 0, \tag{3}$$

where $d/dt = \partial/\partial t + \Omega\partial/\partial\lambda + u\partial/\partial r$ and $\zeta' = \partial rv'/r\partial r - \partial u'/r\partial\lambda$ is the vertical component of the perturbation relative vorticity. The total PV in Eq. (3) can be rewritten as

$$\frac{\overline{\eta} + \zeta'}{H + h'} = \frac{\overline{\eta} + \zeta'}{H(1 + h'/H)} \approx \frac{\overline{\eta} + \zeta'}{H}\left(1 - \frac{h'}{H}\right).$$

After neglecting the second-order perturbation term, we obtain the following linearized shallow-water PV equation for perturbations:

$$\left(\frac{\partial}{\partial t} + \overline{\Omega}\frac{\partial}{\partial\lambda}\right)\left(\frac{\zeta'}{H} - \overline{q}\frac{h'}{H}\right) + u'\frac{d\overline{q}}{dr} = 0, \tag{4}$$

where $\overline{q} \equiv \overline{\eta}/H$ is the basic-state PV and the perturbation PV may be defined as $q' \equiv (\zeta' - \overline{q}h')/H$. It can be readily shown that ζ' and $\overline{q}h'$ (or D'), denoting the respective rotational and divergent components of wave motions, are of the same order of magnitude (i.e., $\zeta' \sim D'$) in intense TCs. This may be achieved by performing a scale analysis of Eq. (2c) and assuming $\overline{\eta} \sim \overline{\Omega}$, so that $\overline{\eta}h' \sim HD'$ or $\overline{q}h' \sim D'$. It is evident that if the wave motion is nondivergent (i.e., $H \to \infty$), Eq. (4) will degenerate to

$$\left(\frac{\partial}{\partial t} + \overline{\Omega}\frac{\partial}{\partial\lambda}\right)\zeta' + u'\frac{d\overline{\eta}}{dr} = 0, \tag{5}$$

which is the linearized barotropic vorticity equation used by MK97 to develop the well-known VRW theory. Because the radial gradient of the mean absolute vorticity (i.e., $\beta_0 \equiv d\overline{\eta}/dr$) in Eq. (5) is analogous to the β effect in the classic Rossby-wave theory, VRWs may propagate in TCs.

One can see from Eqs. (3) and (4) that under the constraint of PV conservation, any alteration in q may result in changes in both ζ' and h', corresponding to the formation and propagation of VRWs and IGWs, respectively. Apparently, the VRW solution, derived from the barotropic vorticity Eq. (5), is a special solution of Eq. (4). It follows that under the PV conservation constraint, VRWs and IGWs may coexist to form the mixed VRIGWs. Whether or not they are inseparable waves remains to be examined after obtaining the associated frequency equations in the next section.

It should be mentioned that Eqs. (2a)–(2c) were also used by MK97 to derive a local dispersion relation in terms of the mean radial PV gradient with the divergence effects included. However, because of their use of the filtered asymmetric balance theory of Shapiro and Montgomery (1993), only one wave frequency solution, similar to (1), was obtained. As will be seen next, Eqs. (2a)–(2c) should give rise to three wave solutions, two of which are associated with the vortex IGWs and the mixed VRIGWs. In fact, SM04 found solutions for VRWs and IGWs from a complete system of the hydrostatic equations with stratification included, but their solutions show the propagations of VRWs and IGWs only in the inner core and outer regions, respectively.

3. Wave frequency equations

Assuming that the spatial and temporal dependence of u' may be separated by specifying solutions in the form of azimuthally propagating waves, then

$$u' = \tilde{u}(r)\exp[i(n\lambda - \hat{\omega}t)] + \text{c.c.}, \tag{6}$$

where $\tilde{u}(r)$ is the wave amplitude of radial wind, and $\hat{\omega}$ is the local wave frequency at $r = r_0$ (likewise for v' and h'). Because the radial length scale of the waves is much shorter than the characteristic radius of a TC vortex, some basic-state variables may be assumed, following MK97, to be slowly varying and they can be expanded in series; for example,

$$\begin{cases} \overline{\Omega} = \overline{\Omega}_0 + \Delta r\, d\overline{\Omega}_0/dr + \cdots \\ \dfrac{d\overline{\eta}}{dr} = \dfrac{d\overline{\eta}_0}{dr} + \Delta r\, d^2\overline{\eta}_0/dr^2 + \cdots \\ \dfrac{1}{r} = \dfrac{1}{r_0}\left(1 - \dfrac{\Delta r}{r_0} + \cdots\right), \end{cases}$$

where $\Delta r = r - r_0$, and r_0, $\overline{\Omega}_0$, $d\overline{\eta}_0/dr$ as well as the other variables with the subscript "0", will be treated as

constants around $r = r_0$. After eliminating v' and h' (see the appendix), we obtain a second-order ordinary differential equation in the unknown variable $\tilde{u}$:

$$\frac{d^2\tilde{u}}{dr^2} + \left(\frac{1}{r} + \frac{\kappa g}{c_0^2}\frac{dH}{dr}\right)\frac{d\tilde{u}}{dr} + \left(\frac{\overline{\omega}^2}{c_0^2} - \frac{1}{r^2} + \frac{\kappa g}{c_0^2}\frac{d^2H}{dr^2} + r\frac{\overline{\eta}_0}{c_0^2}\frac{d\overline{\Omega}_0}{dr} - \frac{\overline{\eta}_0^2}{c_0^2} - \frac{n^2}{r^2} + \frac{n}{r\overline{\omega}}\frac{d\overline{\eta}_0}{dr} - \frac{2n}{\overline{\omega}r^2}\overline{\eta}_0 - \frac{\kappa g n\overline{\eta}_0}{c_0^2\overline{\omega}r}\frac{dH}{dr}\right)\tilde{u} = 0, \quad (7)$$

where $\overline{\omega} = \hat{\omega} - \overline{\Omega}_0 n \neq 0$ and $c_0 = \sqrt{gH}$ is the phase velocity of surface gravity waves and is considered to be constant. Equation (7) is a homogeneous equation, so we may expect that nontrivial solutions satisfying appropriate boundary conditions will exist for certain values of $\overline{\omega}$ corresponding to the frequencies of normal-mode waves. However, Eq. (7) is too complicated for deriving the wave frequency equations because the coefficients for $d\tilde{u}/dr$ and $\tilde{u}$ are not constants but functions of r. Thus, it is desirable to explore whether Eq. (7) can be simplified or transformed into an ordinary differential equation with constant coefficients.

As a first step, let us examine if Eq. (7) could be realistically simplified by estimating the relative magnitudes of basic-state variables with a cloud-resolving simulation of Hurricane Andrew (1992) at the finest grid size of 2 km (see Yau et al. 2004; Liu et al. 1997). Because the most intense rotation occurs near the top of the boundary layer in the eyewall, the model-simulated variables will be azimuthally and vertically averaged in the 900–800-hPa layer, followed by 2-h temporal averages during the mature stage of Andrew in order to obtain more representative basic-state quantities (see Fig. 1). The 900–800-hPa layer, which is equivalent to a depth (H) of about 1 km, is used for the present study of mixed VRIGWs because of the assumed same order of magnitude for rotation and divergence, according to the scale analysis of the continuity equation (i.e., $H \sim W/D$, where $W \sim 10^{-1}$ m s^{-1} and $D' \sim 10^{-4}$ s^{-1}). Figure 1a shows that the radial distribution of $H(r)$ increases from 800 m at the center to 1400 m in the outer region. Its radial variation (i.e., dH/dr) is more than one order of magnitude smaller than H/r (see Fig. 1c) except near the radius of maximum wind (RMW) (at $r = 40$ km, see Fig. 1a). Thus, we may assume $g\,dH/dr \ll c_0^2/r$ and neglect the advection of the mean height by perturbation radial flows by setting $\kappa = 0$ in Eq. (7). In addition, for the sake of subsequent scaling, we assume that $\overline{\omega}$ is of the same order of magnitude as $\overline{\eta}_0$, so the last term in the final set of parentheses can be simplified. With the above approximations, Eq. (7) can then be rewritten as

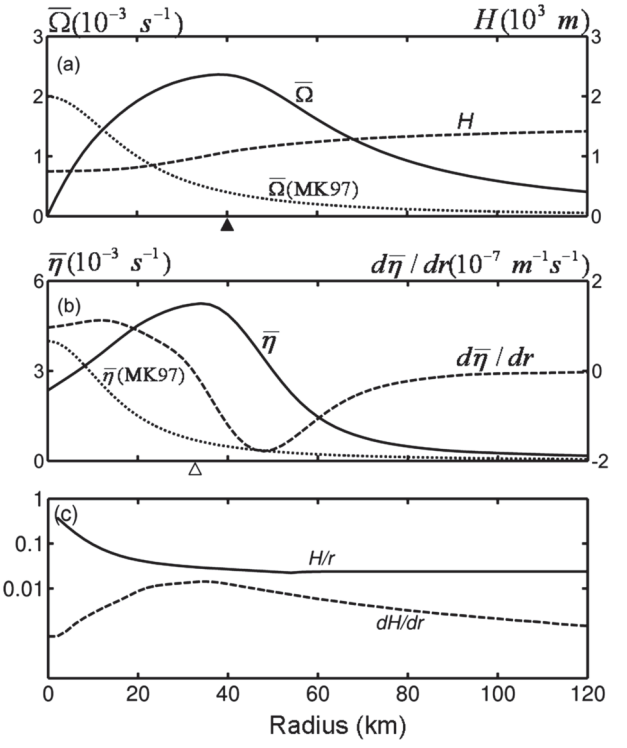

FIG. 1. Radial profiles of the temporally averaged basic-state variables from the 62–64-h simulations of Hurricane Andrew (1992) with the finest grid size of 2 km (see Yau et al. 2004; Liu et al. 1997), then azimuthally and vertically averaged in the 900–800-hPa layer: (a) Angular velocity ($\overline{\Omega}$, solid, 10^{-3} s^{-1}) and mean height (H, dashed, 10^3 m); (b) vertical absolute vorticity ($\overline{\eta}$, solid, 10^{-3} s^{-1}), and its radial gradient ($d\overline{\eta}/dr$, dashed, 10^{-7} m^{-1} s^{-1}); and (c) H/r (solid) and dH/dr (dashed) with logarithmical ordinate. Dotted lines in (a) and (b) denote the angular velocity and the vertical absolute vorticity used by MK97, respectively. The solid and hollow triangles show the location of the RMW and the RMV, respectively.

$$\frac{d^2\tilde{u}}{dr^2} + \frac{1}{r}\frac{d\tilde{u}}{dr} + \left(\frac{\overline{\omega}^2}{c_0^2} - \frac{1}{r^2} + \frac{r\overline{\eta}_0}{c_0^2}\frac{d\overline{\Omega}_0}{dr} - \frac{\overline{\eta}_0^2}{c_0^2} - \frac{n^2}{r^2} + \frac{n\,d\overline{\eta}_0/dr}{r\overline{\omega}} - \frac{2n}{r^2}\right)\tilde{u} = 0. \quad (7')$$

Next, we define a set of characteristic scaling parameters using the model simulation as given in Fig. 1 in order to transform Eq. (7′) to a standard type of ordinary differential equation. These parameters include the RMW ($R_m \sim 4 \times 10^4$ m), the equivalent mean depth for shallow water gravity waves ($H \sim 10^3$ m), the angular velocity ($\Omega_m \sim 10^{-3}$ s^{-1}), and the absolute vorticity ($\overline{\eta}$, $\Omega_m \sim 10^{-3}$ s^{-1}). With these scaling parameters, we define the following nondimensional parameters:

$$r = R_m R, \quad \overline{\Omega}_0 = \Omega_m \Omega, \quad \overline{\eta}_0 = \Omega_m \eta, \quad \overline{\omega} = \sqrt{\beta_0 c_0}\,\omega, \quad (8)$$

where R, Ω, η, and $\omega(\sim\eta)$ denote the nondimensional radius, angular velocity, vertical absolute vorticity, and wave frequency, respectively.

In addition, we introduce two more nondimensional quantities: the Froude number, $F_r = \Omega_m^2 R_m^2/gHR_m^2$, as the ratio of the squared rotational speed to the squared phase speed of surface gravity waves (Ford 1994); and the vortex Rossby number, $R_0 = \Omega_m/(R_m|\beta_0|)$, as the ratio of the basic-state rotation to its radial-mean vorticity. A small value of F_r corresponds to weak rotation or strong divergence associated with gravity waves, whereas a small value of R_0 implies the dominant effects of β_0 on the generation and propagation of VRWs. These two nondimensional quantities are more or less determined by the characteristic scaling parameters of H and β_0 or $\overline{\Omega}$; both are functions of radius. Specifically, $d\overline{\eta}/dr$ decreases from 2×10^{-7} m^{-1} s^{-1} from the TC center to a negligible value near $r = 35$ km and then it changes to negative in the outer region. As a result, R_0 has a small value of 0.2 within the radius of 50 km, but it increases rapidly beyond $r = 60$ km and reaches a value of 14 at $r = 120$ km (Fig. 2b). However, there is a singularity with very large R_0 values inside the RMW (i.e., at $r = 35$ km, see Fig. 1b), hereafter referred to as the radius of maximum vorticity (RMV), due to the presence of $\beta_0 = 0$. This singularity has little effect on our discussions that will follow, apart from the absence of VRWs in accordance with Eqs. (1) and (5). In contrast, F_r decreases slowly with radius (e.g., from 0.22 at the TC center to 0.12 at $r = 120$ km), with an average value of about 0.15 outside the RMW (Fig. 2a). The radial distributions of R_0 and F_r suggest that the inner and outer regions are more favorable for the propagation of VRWs and IGWs, respectively, except in the vicinity of the RMW or RMV.

Note that the basic-state profile used to set up the scaling parameters differs from that used by MK97. That is, the mean angular velocity $\overline{\Omega}$ peaks near the RMW with a finite rotation at the TC center, and then it decreases outward. This is in marked contrast to a hypothetical near-Gaussian swirl profile with the maximum rotation at the TC center in MK97 (see Fig. 1a). This also leads to significantly different profiles of the $\overline{\Omega}$-derived variables such as the absolute vorticity $\overline{\eta}$ and its radial gradient $d\overline{\eta}/dr$ (see Fig. 1b).

Substitution of the above scaling parameters into Eq. (7′) gives the nondimensional form of the radial structure equation in $\tilde{u}$:

$$\begin{cases} R^2 \dfrac{d^2\tilde{u}}{dR^2} + R\dfrac{d\tilde{u}}{dR} + [\tau_1 R^2 - (n+1)^2]\tilde{u} = 0 \\ \tilde{u}|_{R\to 0} = 0, \quad \tilde{u}|_{R\to R_b} = 0 \end{cases}, \qquad (9)$$

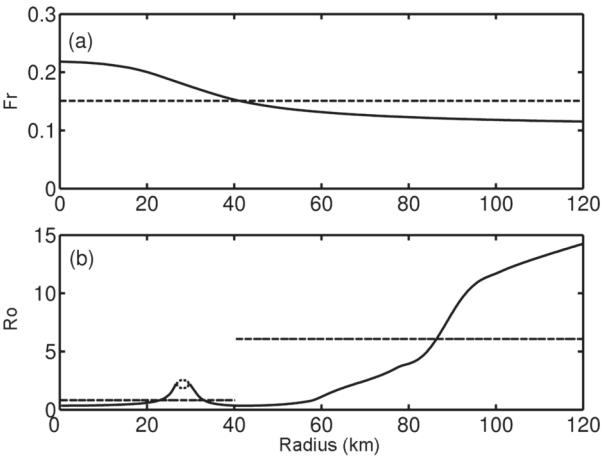

FIG. 2. As in Fig. 1, but for radial distribution of (a) the Froude number, $F_r = \Omega_m^2 R_m^2/gH$, and (b) the vortex–Rossby number, $R_0 = \Omega_m/(R_m\beta_0)$, with dashed lines denoting their radial averages. Note the singularity of R_0 at the RMV (i.e., near $r = 35$ km) in (b).

where $\tau_1 = \omega^2 + nR_0T_r/\omega + F_r\eta\Omega$, $T_r = R^{-1}\, d\eta/dR$; and R_b is the nondimensionized radius at the outmost boundary where little wave energy could be reflected to influence wave activities in the eyewall. Because of some peculiar features of WN-1 VRWs, our subsequent discussions of Eq. (9) will be limited only to waves with $n \geq 2$. Equation (9) is essentially Bessel's equation, so solving it for $\tilde{u}$ can now be regarded as an eigenvalue problem of Bessel's equation, provided that parameter τ_1 can be treated as real positive constant. For the purpose of examining the wave propagation and structures (i.e., assuming $\omega_i = 0$), we plot the radial distribution of τ_1 for nondimensionalized frequency ω in the range of $[-5, 5]$, with $n = 2$ and all the other variables (e.g., η, Ω, $d\eta/dR$) as given in Fig. 1. It is evident from Fig. 3 that for a given ω the radial variation of τ_1 is generally much less than 10%, even at the RMV where R_0 is singular but $|R_0T_r| = \Omega_m/R_mR$ is finite. Moreover, τ_1 varies less for higher frequencies. In fact, a scale analysis indicates that ω^2 is the dominant term in τ_1, and the contribution from the third radius-dependent term is small due to the smallness of F_r. Apparently, setting $\kappa = 1$ in Eq. (7) would affect little the radial variation of τ_1 and our subsequent discussions (but it would not possibly transform the coefficient of $d\tilde{u}/dr$ into a standard form of Bessel's equation). Hence, we may approximate τ_1 as constant in both the inner and outer regions and then obtain the following characteristic equation satisfying the given boundary conditions given in Eq. (9):

$$m^2 \equiv \tau_1 = \omega^2 + \frac{nR_0T_r}{\omega} + F_r\eta\Omega. \qquad (10)$$

This yields a solution (in dimensional form) for the (radially discrete) perturbation radial velocity u':

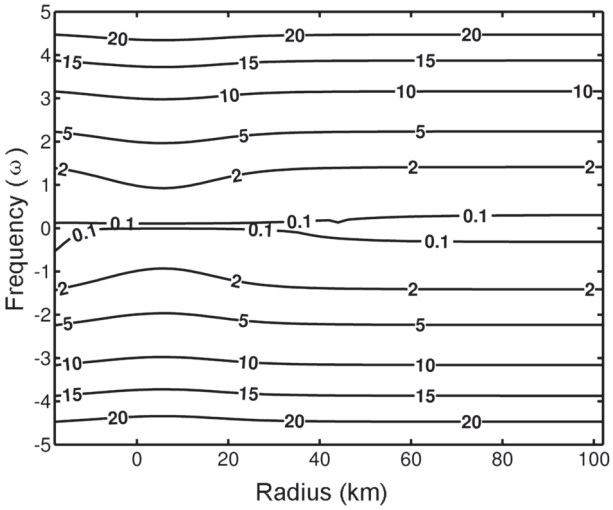

FIG. 3. The frequency–radius (ω–r) distribution of Bessel's parameter τ_1 for wavenumber $n = 2$ (see text), based on the basic-state profiles given in Figs. 1 and 2.

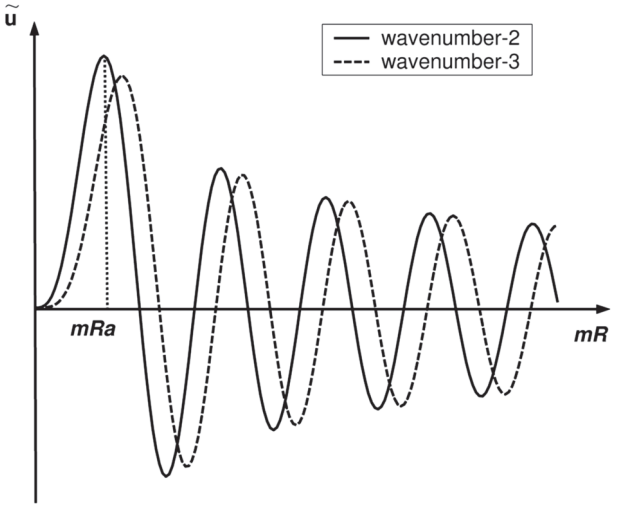

FIG. 4. Radial distribution of the amplitude of the perturbation radial wind—that is, $\tilde{u}(r) = u_0 J_{n+1}(mR)$, where $u_0 = 1$ m s^{-1}—for wavenumber $n = 2, 3$ obtained from Bessel's function of the first kind [see Eq. (11)]; R_a denotes the radius of peak radial wind.

$$u' = u_0 J_{n+1}\left(\frac{mr_0}{R_m}\right)\exp[i(n\lambda - \hat{\omega}t)] \quad (n = 1, 2, 3, \ldots), \tag{11}$$

where u_0 is the amplitude of perturbation radial velocity u', $u_0 J_{n+1}(mR)$ denotes the radial amplitude distribution of u', $m = \sqrt{\tau_1} = \mu_j/R_b (j = 1, 2, 3, \ldots)$, or μ_j is the node of the nth-order Bessel function of the first kind; that is,

$$J_n(mR) = \sum_{k=0}^{\infty}(-1)^k \frac{1}{k!\Gamma(n+k+1)}\left(\frac{mR}{2}\right)^{n+2k}. \tag{12}$$

That is, μ_j corresponds to each positive root of $J_{n+1}(\mu_j) = 0$ that is a function of the azimuthal WN-n for a given boundary radius (R_b). Thus, we have $\mu_j \equiv \mu_j(n)$, and $m \equiv m(n)$ for a given wave frequency ω. Like $(gH_e)^{-1}$, which is an eigenvalue for the vertical structure equation when the shallow-water equations are applied to a stratified fluid with equivalent depth (H_e) (see Daley 1981), the radial eigenvalue $\overline{m} = m(n)/R_m$ is the percentage distance of each node from the TC center with respect to the RMW (R_m) for a given WN-n. In essence, $\overline{m}$ is equivalent to a radial WN. The index k gives alternating signs between the nodes with decreasing amplitudes for larger n.

Figure 4 shows the radial distributions of wave amplitudes for WN-2 and WN-3 calculated from $u_0 J_{n+1}(mR)$. We see that (a) the wave amplitude decreases with increasing n and r, indicating that more wave energy is concentrated in longer waves and in the inner-core region, and (b) each azimuthally propagating wave has a radius of maximum amplitude (R_a) that is larger for higher n, suggesting that fewer (more) contributions from shorter waves occur in the inner (outer) region. Furthermore, the wave amplitude is null at the TC center, peaks at R_a, and then decreases, while oscillating, with radius in the outer region. Of interest is that longer waves decay at rates faster than shorter waves in the inner region; they all decay at much slower rates in the outer region. Overall, Eq. (12) provides a summation of all allowable "radially standing" perturbations associated with azimuthally propagating waves.

With the radial eigenvalue of m known from the Bessel equation, we can now solve the characteristic Eq. (10), which is essentially a cubic frequency equation for allowable waves with azimuthal WN n; that is,

$$F(\omega) = \omega^3 - (m^2 - F_r\eta\Omega)\omega + nR_0T_r = 0. \tag{13}$$

Clearly, there are three possible wave frequency solutions, depending on the sign of Q from the following discriminant equation (Zwillinger 2003):

$$Q = \frac{(m^2 - F_r\eta\Omega)^3}{27} - \frac{1}{4}n^2R_0^2T_r^2. \tag{14}$$

Equation (13) can be solved graphically with all possible values of the variables on the rhs of Eq. (14), which would lead to three different signs of Q. When $Q > 0$, we can see from Fig. 5 that the curve of $F(\omega)$ intersects the ω axis at three points, implying the existence of three distinct real roots. Two of them are for high-frequency (ω_1, ω_3) waves propagating azimuthally in opposite directions, and the third one is for a low-frequency (ω_2)

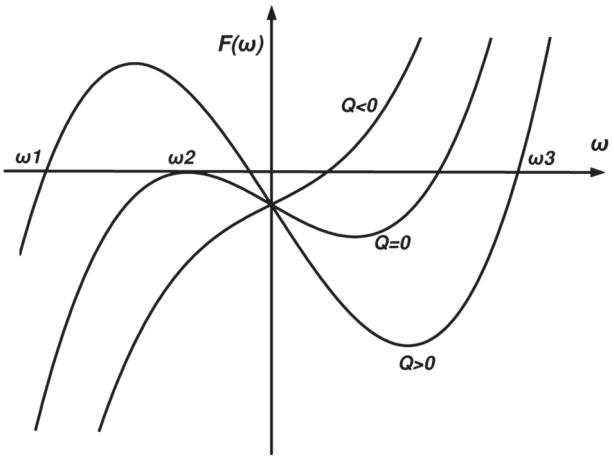

FIG. 5. Allowable (real or complex) wave solutions from the cubic frequency Eq. (13), that is, $F(\omega) = 0$, that are dependent on the sign of Q in Eq. (14), according to the basic-state profiles given in Figs. 1 and 2, assuming $\omega_1 < \omega_2 < 0 < \omega_3$.

wave propagating against the mean flow. When $Q = 0$, there are two intersections of the $F(\omega)$ curve with the ω axis, one of which corresponds to two identical negative roots. This indicates that the cyclonic-propagating high-frequency (ω_3) wave will be shifted to a lower frequency, whereas the anticyclonic-propagating high- (ω_1) and low- (ω_2) frequency waves are reduced to an intermediate frequency. When $Q < 0$, there are both a single real solution (ω_3), corresponding to a cyclonic-propagating low-frequency wave, and two complex conjugate solutions (ω_1, ω_2) associated with dynamically unstable waves. Let us now examine what the three groups of solutions are.

a. The $Q > 0$ solutions

The three real solutions can be easily separated by assuming high-frequency waves, so nR_0T_r in Eq. (13) can be omitted to give the following local dispersion relation:

$$\omega_{1,3} \approx \pm\sqrt{m^2 - F_r\eta\Omega}. \tag{15}$$

Converting it back to dimensional form gives

$$\hat{\omega}_G = \overline{\Omega}_0 n \pm \sqrt{c_0^2\overline{m}^2 - \overline{\eta}_0\overline{\Omega}_0}, \tag{15′}$$

where $\overline{m} = m(n)/R_m$. Equation (15′) represents clearly high-frequency IGWs that are influenced by the rotational flows of TCs through $\overline{\eta}_0\overline{\Omega}_0$. Thus, we may refer them to as vortex IGWs propagating oppositely in the rotational flows of TCs, whose phase velocities are

$$c_G = \overline{\Omega}_0 r_0 \pm \frac{r_0}{n}\sqrt{c_0^2\overline{m}^2 - \overline{\eta}_0\overline{\Omega}_0}. \tag{16}$$

Equation (16) states that azimuthally propagating vortex IGWs tend to be slower in the regions of more rapid rotation and higher absolute vorticity than typical IGWs. In addition, the higher the azimuthal wavenumber, the more slowly the vortex IGWs will propagate.

Similarly, the dispersion relation for the low-frequency waves can be obtained by neglecting the term ω^3 in Eq. (13):

$$\omega_2 \approx \frac{nR_0T_r}{m^2 - F_r\eta\Omega}. \tag{17}$$

Converting it to dimensional form gives the dispersion relations for the low-frequency waves:

$$\hat{\omega}_R = \overline{\Omega}_0 n + \frac{n\beta_0}{r_0(\overline{m}^2 - \overline{\eta}_0\overline{\Omega}_0/c_0^2)}. \tag{17′}$$

Equation (17′) is similar to the dispersion relation (1) associated with azimuthally propagating VRWs in MK97 if $\overline{m}^2 = n^2/r_0^2$ and without the influence of gravity and mean rotation. This implies again that the VRW discussed by MK97 is a special type of the low-frequency waves in the above solution. Then, the phase velocity of the "modified" VRWs can be expressed as

$$c_R = \frac{r_0\hat{\omega}_R}{n} = \overline{\Omega}_0 r_0 + \frac{\beta_0}{\overline{m}^2 - \overline{\eta}_0\overline{\Omega}_0/c_0^2}. \tag{18}$$

Because cyclonic rotation is defined as positive in polar (r, λ) coordinates, azimuthally propagating VRWs will be faster (slower) than the mean flows inside (outside) the RMW because of the sign of β_0.

b. The $Q = 0$ solutions

In the $Q = 0$ case, we have the Cardan solutions (Zwillinger 2003) to the frequency Eq. (13); that is,

$$\begin{cases} \hat{\omega}_- = \overline{\Omega}_0 n - \sqrt[3]{4nc_0^2\beta_0/r_0} \\ \hat{\omega}_+ = \overline{\Omega}_0 n + \sqrt[3]{0.5nc_0^2\beta_0/r_0} \end{cases}, \tag{19}$$

where $\hat{\omega}_-$ and $\hat{\omega}_+$ represents two allowable waves propagating against and with the mean rotational flows, respectively, corresponding to two identical negative roots (ω_1, ω_2) and one positive root (ω_3) (see Fig. 5). One may note that both $\hat{\omega}_-$ and $\hat{\omega}_+$ will approach $\overline{\Omega}_0 n$ as either $\beta_0 \to 0$ or $c_0 \to 0$. Since β_0 and c_0 are closely related to VRWs and gravity waves, respectively, and since they are inseparable from (19), both $\hat{\omega}_-$ and $\hat{\omega}_+$ may be considered as the frequencies of mixed VRIGWs. The two mixed waves are similar in physical properties

to the equatorial Rossby–gravity waves discovered by Matsuno (1966) in which the gravitational and earth curvature effects could not be separated. Clearly, these mixed waves differ from those with the $Q > 0$ solutions in which VRWs and IGWs can be isolated.

c. The $Q < 0$ solutions

Under the $Q < 0$ condition, Eq. (13) has the following three solutions:

$$\begin{cases} \omega_3 = \omega_A + \omega_B, \\ \omega_{1,2} = -(\omega_A + \omega_B)/2 \pm i\sqrt{3/4}(\omega_A - \omega_B), \end{cases}$$

where ω_3 is a real frequency, $\omega_{1,2}$ are complex conjugate frequencies, and

$$\omega_A = \sqrt[3]{-nR_0T_r/2 + \sqrt{(n^2R_0^2T_r^2/4) - (m^2 - F_r\eta\Omega)^3/27}},$$

$$\omega_B = \sqrt[3]{-nR_0T_r/2 - \sqrt{(n^2R_0^2T_r^2/4) - (m^2 - F_r\eta\Omega)^3/27}}.$$

Their corresponding dimensional dispersion relations can be expressed as

$$\hat{\omega}_3 = \overline{\Omega}_0 n - (\hat{\omega}_A + \hat{\omega}_B), \tag{20a}$$

$$\hat{\omega}_{1,2} = \overline{\Omega}_0 n - \left(\frac{\hat{\omega}_A + \hat{\omega}_B}{2}\right) \pm i\sqrt{\frac{3}{4}}(\hat{\omega}_A - \hat{\omega}_B), \tag{20b}$$

where

$$\hat{\omega}_A = \sqrt[3]{(-0.5nc_0^2\beta_0/r_0) + \sqrt{(n^2\beta_0^2c_0^4/4r_0^2) - (\overline{m}^2c_0^2 - \overline{\eta}_0\overline{\Omega}_0)^3/27}},$$

$$\hat{\omega}_B = \sqrt[3]{(-0.5nc_0^2\beta_0/r_0) - \sqrt{(n^2\beta_0^2c_0^4/4r_0^2) - (\overline{m}^2c_0^2 - \overline{\eta}_0\overline{\Omega}_0)^3/27}}.$$

One can see that both $\beta_0 \to 0$ and $c_0 \to 0$ will give $\hat{\omega}_A \to \sqrt{\overline{\eta}_0\overline{\Omega}_0/3}$, and $\hat{\omega}_B \to -\sqrt{\overline{\eta}_0\overline{\Omega}_0/3}$, so $\hat{\omega}_3 \approx \overline{\Omega}_0 n - (\hat{\omega}_A + \hat{\omega}_B) = \overline{\Omega}_0 n$, and $\hat{\omega}_{1,2} = \overline{\Omega}_0 n - 0.5(\hat{\omega}_A + \hat{\omega}_B) \pm i\sqrt{\overline{\eta}_0\overline{\Omega}_0} = \overline{\Omega}_0 n \pm i\sqrt{\overline{\eta}_0\overline{\Omega}_0}$. Clearly, Eq. (20) represents three solutions of inseparable mixed VRIGWs. Of particular interest is that $\hat{\omega}_{1,2}$ includes both the propagating and the growing (decaying) modes of the mixed VRIGWs, with a mean-flow speed and a growth (decaying) rate on the order of $\sqrt{\overline{\eta}_0\overline{\Omega}_0}$. This implies the presence of the mixed-VRIGW instability in TCs when the criterion of $Q < 0$ is met. As for the sole real solution $\hat{\omega}_3$, Fig. 5 shows that it is a lower-frequency mixed VRIGW that differs in sign and magnitude from that under the condition of $Q = 0$ but contains some common characteristics associated with VRWs and IGWs, as described by Eqs. (15′) and (17).

Note that although $\omega_{1,2}$ are complex conjugate frequencies under the conditions of $Q < 0$, they are still the characteristic modes of Eq. (9) that satisfy $\tau_1 = m^2 > 0$. However, when the basic state becomes dynamically unstable, as in the study of SM04, the Bessel function cannot provide a complete description of both the wave instability and propagation. Thus, we may use $\tilde{u}^{(1)} \sim H_{n+1}^{(1)}(mR)$ and $\tilde{u}^{(2)} \sim H_{n+1}^{(2)}(mR)$ as the two linearly independent solutions of Eq. (9), where $H_{n+1}^{(1)}(mR) = J_{n+1}(mR) + iY_{n+1}(mR)$ and $H_{n+1}^{(2)}(mR) = J_{n+1}(mR) - iY_{n+1}(mR)$ are the $(n + 1)$th-order Hankel function of the first and second kind, respectively, corresponding to the growing and decaying solutions of Eq. (9); and $Y_{n+1}(mR) = [J_{n+1}(mR)\cos(n+1)\pi - J_{-(n+1)}(mR)]/\sin(n+1)\pi$ is the $(n + 1)$th-order Bessel function of the second kind. Because of the property of $Y_{n+1}(mR) \to -\infty$ as $R \to 0$, $Y_{n+1}(mR)$ does not satisfy typical boundary conditions in the TC core region. SM04 circumvented this problem by assuming $\tilde{u}_0 \sim R^n$ for the core region and then iteratively solved a second-order ordinary differential equation, similar to Eq. (9) but with variable coefficients, for the dominant complex frequencies. In their studies (e.g., SM04; Schecter and Montgomery 2003, 2007), azimuthally propagating waves are treated as VRWs in accordance with the nondivergent dispersion relation of MK97, whereas vertically propagating waves are viewed as internal IGWs. As mentioned above, the horizontally propagating waves are inseparable mixed waves in restoring forces when intense rotation and divergence are both present in the TC core region. In the next section, we will discuss the formation and propagation mechanisms of the mixed waves. Their associated instability problems, as compared to those of SM04, will be examined in a future study.

4. Wave dynamics

We have shown in the preceding section that after including both rotational and divergent components in

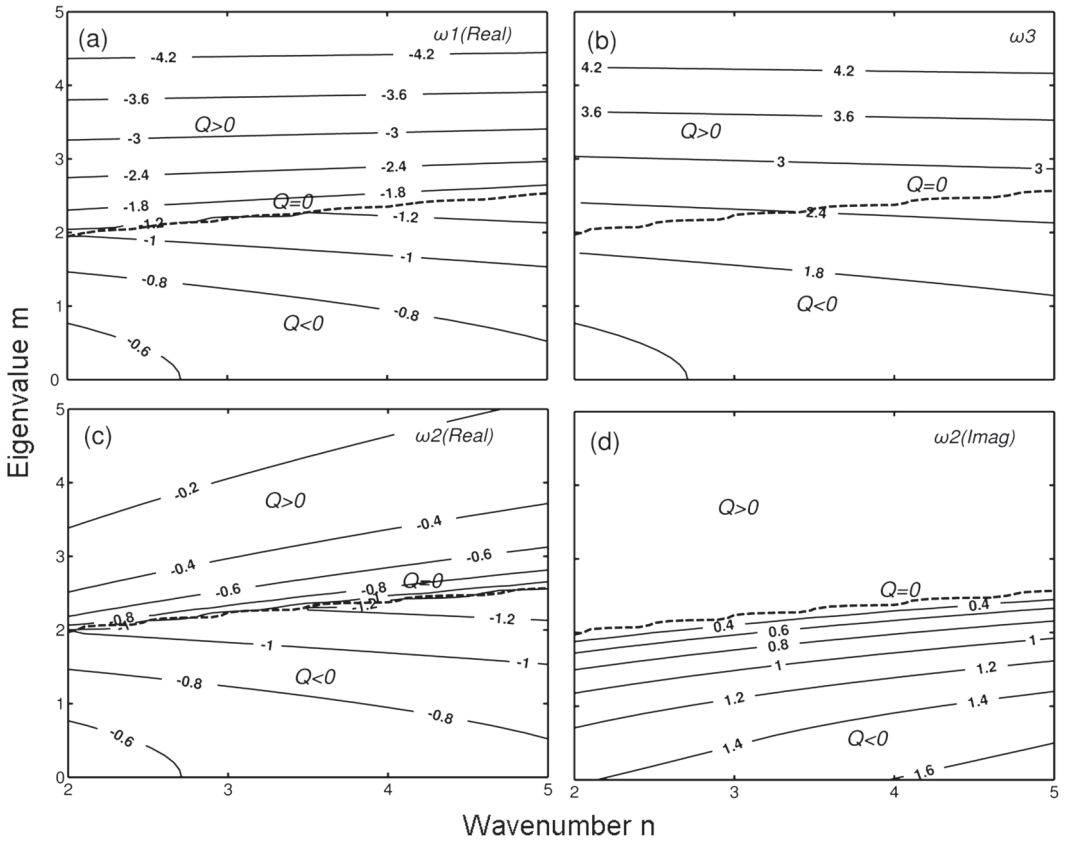

FIG. 6. Frequency (ω) diagrams as functions of the radial eigenvalue (m) and wavenumber (n) for (a) ω_1 against-flow gravity waves ($Q > 0$) and propagating mixed VRIGWs ($Q \leq 0$); (b) ω_3 along-flow gravity waves; (c) ω_2 against-flow VRWs ($Q > 0$) and propagating mixed VRIGWs ($Q \leq 0$); and (d) ω_2 unstable mixed VRIGWs ($Q < 0$). The ω isopleths are given at intervals of 0.2 and 0.6 for high- and low-frequency waves, respectively. They are calculated from Eq. (13) with the averaged quantities between the radial range of 30 and 60 km (e.g., $R_0 = 0.5$, $F_r = 0.15$, $T_r = -2$, $\Omega = 2$, and $\eta = 3$). Dashed lines denote the distribution of $Q = 0$ with m and n, based on Eq. (14).

the shallow-water equations model, there are a total of eight allowable wave solutions, depending on the sign of Q. The wave solutions are much more complicated than those associated with simple VRWs or IGWs. Thus, it is desirable to examine what dynamical characteristics of these waves are, including the parameters that determine the sign of Q, the regions where these waves will likely develop in TCs, and their pressure–wind relations and propagating structures.

a. Wave dispersion characteristics

For the convenience of our subsequent discussion, we may assume that the real-part solutions of Eq. (13), as shown in Fig. 5, satisfy the following relation:

$$\omega_1 < \omega_2 < 0 < \omega_3,$$

where ω_1 and ω_3 are high-frequency waves propagating against and along the mean flow, respectively, and ω_2 is a low-frequency wave propagating against the mean flow. By specifying the basic-state variables of R_0, F_r, T_r, Ω, and η with the given eigenvalue of m, we can obtain the characteristic frequencies (ω_1, ω_2, ω_3) as a function of WN n from Eq. (13). These basic-state variables also determine the sign of Q, leading to different wave characteristics.

Figure 6 shows such frequency diagrams for anticyclonically ω_1- and cyclonically ω_3- propagating waves (Figs. 6a and 6b, respectively), as well as the real (Fig. 6c) and imaginary part (Fig. 6d) of the low-frequency anticyclonically propagating ω_2 waves in a selected region in the eyewall. First, just like the equivalent depth, the radial eigenvalue m from Bessel equation is closely related in magnitude to wave frequency, especially for high-frequency waves. Lower-frequency waves tend to have fewer radial nodes or ''standing'' structures. Second, higher-frequency waves (e.g., $\omega > 2$) exhibit much less variation in frequency in the WN 2–5 range (i.e., with more horizontally oriented isofrequency contours), suggesting that they are less dispersive and more related to IGWs. Third, as the wave frequency decreases, the Q value decreases (also see Fig. 5) and the wave

dispersion becomes more significant, as indicated by more right- and downward-sloping isofrequency contours with increasing curvature, implying the increasing roles of VRWs in the formation of mixed VRIGWs. Fourth, note the different transitions in dispersion properties (i.e., propagation versus dynamic stability) for the ω_1, ω_2, and ω_3 waves as Q switches from a positive to a negative sign (see Figs. 6a–c). For example, along-flow ω_3 waves vary smoothly with n, such as when crossing the $Q = 0$ line (Fig. 6c). In contrast, anticyclonically propagating ω_1 waves change more abruptly the orientation of isofrequency contours after shifting across the $Q = 0$ line at lower frequencies (Fig. 6b), suggesting more dominant mixed-wave properties in the regions of $Q \leq 0$.

The low-frequency against-flow ω_2 waves are worthy of separate consideration because, as mentioned earlier, they are VRWs, mixed VRIGWs, and dynamically unstable when Q is greater than, equal to, and less than zero, respectively. Of interest is that the $Q = 0$ line corresponds to the highest frequency the mixed VRIGWs could have, given n and m (Fig. 6d); it is $\omega = 0.6 \sim 1.6$ corresponding to a frequency range of 10^{-4}–10^{-3} s^{-1} in the inner region. The mixed-wave instability could only occur with the eigenvalue of $m < 2$, basically at the frequencies of VRWs (Figs. 6c,d). This suggests that when VRWs become highly rotational in the presence of intense latent heat release, they could experience the mixed-wave instability. Of further interest is that the growth rate of the mixed VRIGWs increases with WN (Fig. 6d), implying that shorter waves tend to grow faster than longer waves. Moreover, shorter unstable mixed waves are less dispersive than the corresponding stable VRWs (Fig. 6c). Note that the frequency range shown in Fig. 6 is similar to that of Hodyss and Nolan (2008), who showed the coexistence of unstable modes of VRWs and IGWs. In their study, however, the VRWs and IGWs have separable restoring forces, whereas the two waves shown here are mixed with inseparable wave properties.

We have seen from Eq. (14) that the criteria for different wave solutions and mixed-wave instability depend critically on the sign of Q, which is determined by the radial eigenvalue (m), and some basic-state variables (i.e., F_r, R_0, η, Ω, and T_r); these variables are all functions of radius and azimuthal WN (n). Thus, it is natural to examine to what extent the wave solutions so derived make sense when they are applied to realistic TCs. For this purpose, Fig. 7 shows the distribution of Q as a function of radius for the two long waves (i.e., $n = 2, 3$), with all the basic-state variables specified from the model atmosphere as given in Figs. 1 and 2. An eigenvalue of $m = 1.5$ is used in plotting Fig. 7 because around this value the sign of Q changes with different dynamical

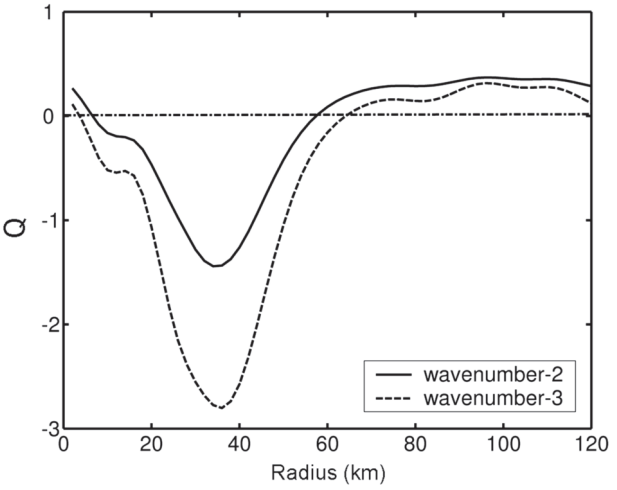

FIG. 7. Radial distribution of the discriminant Q for wavenumber $n = 2$, 3 and $m = 1.5$ [see Eq. (14)], according to the basic-state profiles given in Figs. 1 and 2.

stability regimes for these waves (see Fig. 6). It is of interest that the condition of $Q > 0$ occurs in both the core (i.e., $r < 10$ km) and outer ($r > 60$ km) regions where little diabatic heating is present, whereas $Q < 0$ takes place within the annulus of 10 km $< r <$ 60 km, roughly in the eyewall convective region (Fig. 7). This implies that the eye and outer regions allow for the coexistence of VRWs and IGWs with separable physical characteristics, whereas the eyewall region favors the development of mixed-wave instability, with possible wave instability taking place first in the vicinity of the RMV.

One can see from Eq. (14) that $Q < 0$ occurs in the eyewall mainly because of the presence of large vorticity (or PV) gradients and divergence (or small equivalent depth), suggesting that mixed-wave instability differs from algebraic instability for VRWs discussed by Nolan and Montgomery (2000) and Nolan et al. (2001). Thus, we may state that intense convection in the eyewall accounts for the generation of a favorable basic state for the mixed-wave (ω_1) instability and it is the energy source for the generation of propagating mixed VRIGWs (i.e., ω_3) with both strong rotation and divergence. Obviously, mixed-wave instability appears less likely in weak TCs or during the genesis stage of TCs. Figure 7 also shows that shorter waves tend to experience mixed-wave instability more readily and over wider regions than longer waves. This appears to help explain why polygonal eyewalls as well as multiple vortices could develop in intense TCs (e.g., Schubert et al. 1999; Kossin et al. 2002).

Figure 8 summarizes the characteristic frequencies (ω_1, ω_2, ω_3) of WN-2 and WN-3 waves as functions of

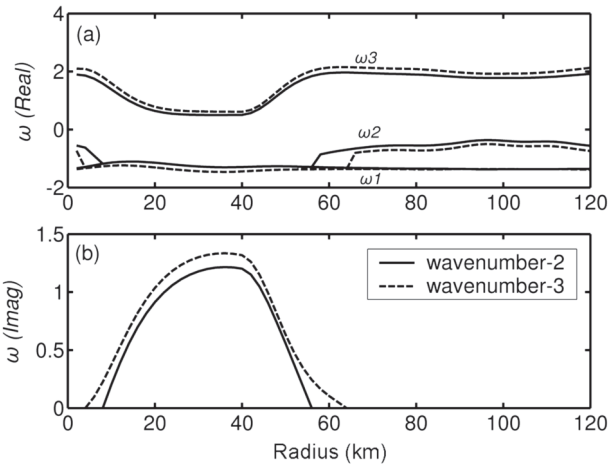

FIG. 8. Radial distribution of (a) the real part ($\omega_1 < \omega_2 < \omega_3$) and (b) the imaginary part (ω_2) of wave frequencies for wavenumber $n = 2$, 3 and $m = 1.5$, according to the basic-state profiles given in Figs. 1 and 2.

radius using the model atmosphere. We can see similar results to those shown in Fig. 7. That is, in the eye and outer regions where $Q > 0$, frequencies ω_1 and ω_3 correspond to a pair of oppositely propagating IGWs, whereas ω_2 represents a low-frequency VRW propagating against the mean flow (Fig. 8a). Moreover, IGWs (i.e., associated with ω_3) propagate in the eyewall region at speeds that are about half of those in the outer region. The result is consistent with the strong unbalanced flows in the eyewall diagnosed by Wang and Zhang (2003) through the PV inversion. In contrast, ω_1 and ω_2 share the same frequency for the mixed VRIGWs propagating in the eyewall (Fig. 8a), but the imaginary part of ω_2 exhibits dynamical growth with the peak rate in the vicinity of the RMV (Fig. 8b). This confirms that the eyewall region near the RMV is more favorable for the rapid growth of mixed VRIGWs or the rapid development of perturbations in both horizontal and vertical directions. Figure 8b also shows that shorter waves grow at rates that are higher than longer waves.

b. Wave propagation characteristics

The two-dimensional propagation characteristics of the abovementioned waves can be examined by substituting the wave frequency equations derived in section 3 into the linearized governing Eqs. (2); see the appendix. That is, substitution of the solution form of (6) for v' and h' into Eq. (A5) and assuming $\kappa = 0$ will give the amplitudes of the perturbation heights and tangential winds:

$$\tilde{h} = \frac{iu_0\Lambda}{2g[(n\overline{\omega}\, d\overline{\Omega}_0/dr) - n^2c_0^2/r_0^3]}, \tag{21a}$$

$$\tilde{v} = \frac{gn}{\overline{\omega}r_0}\tilde{h} - i\frac{\overline{\eta}_0}{\overline{\omega}}\tilde{u}, \tag{21b}$$

where

$$\Lambda = \left[\overline{\omega}^3 - \frac{c_0^2\overline{\omega}}{r_0^2}(n^2+1) + r_0\overline{\eta}_0\overline{\omega}\frac{d\overline{\Omega}_0}{dr} - \overline{\eta}_0^2\overline{\omega} + \frac{n\beta_0c_0^2}{r_0} - \frac{2nc_0^2}{r_0^2}\overline{\eta}_0\right]J_{n+1}\left(\frac{mr_0}{R_m}\right) + \frac{c_0^2m^2\overline{\omega}}{R_m^2}J_{n+3}\left(\frac{mr_0}{R_m}\right),$$

in which the differential properties of Bessel function (i.e., $J'_{n+1} = -J_{n+2}$ and $J''_{n+1} = J_{n+3}$) have been used. By taking the real-part solution, we obtain the following equations for perturbation variables:

$$u' = u_0J_{n+1}\left(\frac{mr_0}{R_m}\right)\cos(n\lambda - \hat{\omega}t), \tag{22a}$$

$$v' = -\frac{u_0}{2[(\overline{\omega}^2 d\overline{\Omega}_0/dr) - n\overline{\omega}c_0^2/r_0^3]} \times \left[\Lambda - \frac{\overline{\eta}_0}{\overline{\omega}}J_{n+1}\left(\frac{mr_0}{R_m}\right)\right]\sin(n\lambda - \hat{\omega}t), \tag{22b}$$

$$h' = -\frac{u_0}{2g[(n\overline{\omega}\, d\overline{\Omega}_0/dr) - n^2c_0^2/r_0^3]}\Lambda\sin(n\lambda - \hat{\omega}t). \tag{22c}$$

One can see from Eq. (22) that (a) u' is a function of r^{n+1} until it reaches a peak value near $R_a = 50$ km (see Fig. 4) at $\lambda = 0, \pi$ and is identical for all the three types of waves at $t = 0$ and that (b) h' and v' are proportional to $\overline{\omega}^2$ and $\overline{\omega}$, respectively, for high-frequency waves but inversely proportional to $\overline{\omega}$ for low-frequency waves, implying that the perturbation height and tangential winds are small for IGWs but large for VRWs. Moreover, since the VRW frequency is proportional to $d\overline{\eta}_0/dr$, as given in Eq. (17′), we have $v' \propto (d\overline{\eta}_0/dr)^{-1}$ so that the amplitude of v' will peak near the RMV where $d\overline{\eta}_0/dr = 0$. By comparison, with an intermediate frequency between an IGW and a VRW (i.e., $\overline{\omega} = -\sqrt[3]{4nc_0^2r_0^{-1}d\overline{\eta}_0/dr}$), a mixed VRIGW has $v' \propto (d\overline{\eta}_0/dr)^{-1/3}$, suggesting that its perturbation tangential wind is much weaker than that for a VRW.

Figure 9 shows an example of the azimuthal propagation of WN-2 perturbation heights and horizontal winds associated with the three types of shallow-water waves as *approximated* by the frequency Eqs. (15), (17), and (20) at $t = 0$ and 1 h; the associated divergence and relative vorticity fields at $t = 0$ h are also provided. Note that because of the use of the approximated dispersion relations, some features may differ slightly from their corresponding pure waves. Nevertheless, different intensities in perturbation heights and winds and different height–wind relations among

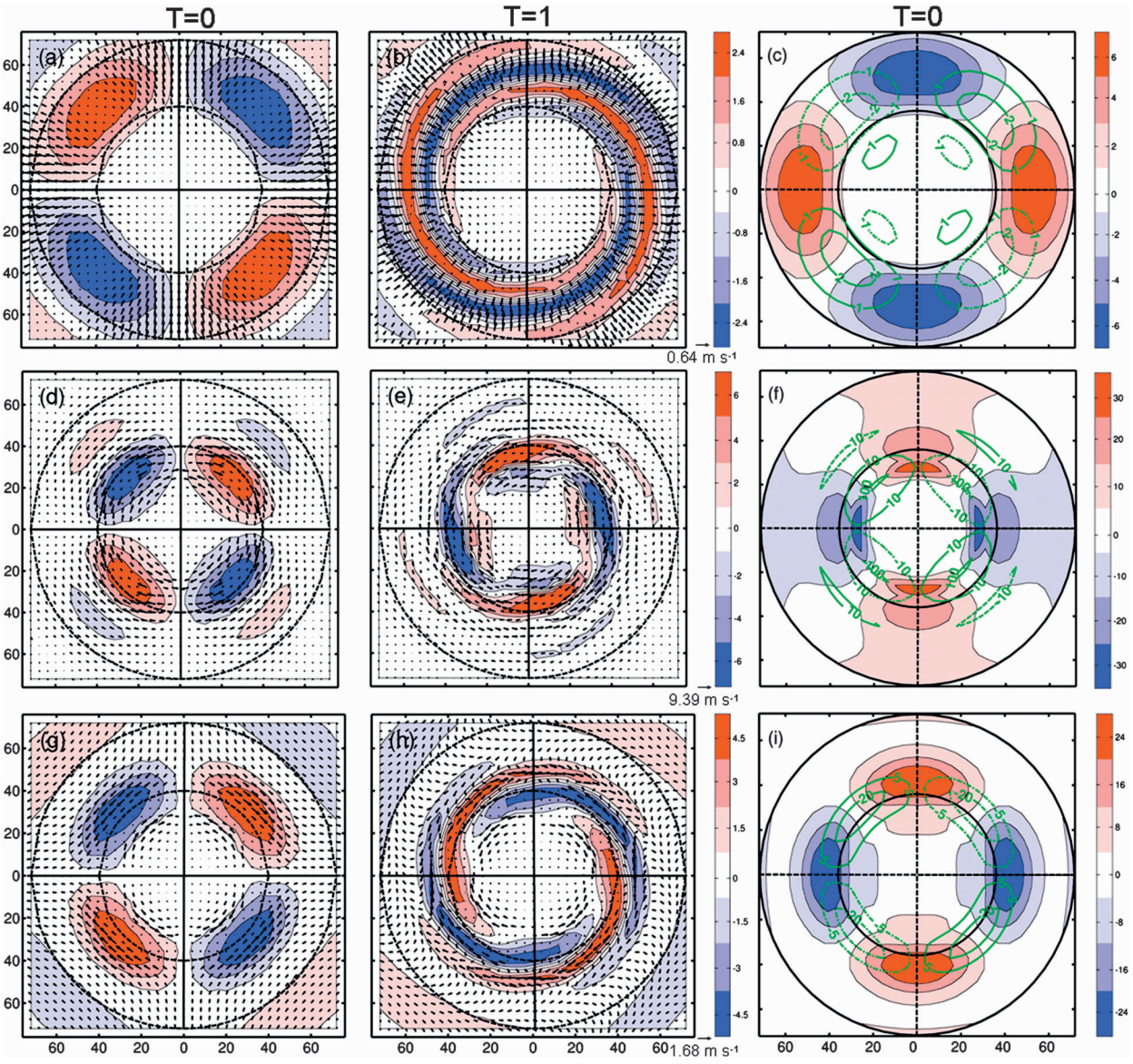

FIG. 9. Horizontal maps of the wavenumber-2 perturbation heights (shadings) and flow vectors at (left) $t = 0$ h, (center) $t = 1$ h, and (right) the relative vorticity (solid/positive, dashed/negative, 10^{-5} s^{-1}) and divergence (shadings, 10^{-5} s^{-1}) associated with (top row) an IGW, (middle row) a VRW, and (bottom row) a mixed VRIGW obtained from Eq. (22) with the approximated frequency Eqs. (15), (17) and (20), respectively. All the other parameters are specified from the model output with $u_0 = 1$ m s^{-1}, and $m = 1.5$ over a domain of 140 km $\times$ 140 km. Note that $\beta_0 = 10^{-7}$ m^{-1} s^{-1} has been used to estimate frequencies at the RMV for the VRW and mixed VRIGW, and vector lengths and shadings for the three different waves denote different values, e.g., with a grid interval representing 0.64, 9.39 and 1.68 m s^{-1} for the peak amplitudes of the IGW, VRW and mixed VRIGW, respectively.

the three WN-2 waves are clearly evident even at the initial time (cf. Figs. 9a, 9d, and 9g). First, horizontal flows are stronger for the VRW and then the mixed VRIGW and IGWs in that order, with a peak amplitude of 9.39, 1.68, and 0.64 m s^{-1}, respectively; similar results are found for their corresponding height perturbations with the respective peak intensities located at a radius slightly outward from the RMV (i.e., $R_a = 36$ km), the RMW (i.e., $R_a = 45$ km), and at the outer edge of the eyewall (i.e., $R_a = 60$ km). The weak tangential flows of the VRW and VRIGW around the RMV are attributable to the use of a small value for β_0 to minimize the influence of singularity. In addition, all the wave amplitudes are small within $r = 10$ km; and both D' and $\zeta' \to 0$, as $r \to 0$, as determined by Bessel's function.

Second, the VRW flows are more azimuthal and rotational, with two couplets of cyclonic and anticyclonic

circulations centered at $R_a = 36$ km, which are similar to those shown in MK97 and Wang (2002). The IGWs' flows are much more radial than azimuthal, and they are also more divergent and across-isobaric, with convergence occurring ahead of (behind) a high (low) (see Fig. 9c). The divergence for the IGWs (VRWs) is 3–4 times greater (smaller) than the relative vorticity (cf. Figs. 9c,f). In contrast, the mixed VRIGWs' flows are both rotational and divergent at similar magnitudes (Fig. 9i), as hypothesized earlier; they are distributed in a radial interval between the VRW and IGW (cf. Figs. 9g, 9a, and 9d). This result is consistent with that given in Fig. 8a showing the generation of mixed IGWs and VRWs primarily in the eyewall region. It is important to note that there are few azimuthally propagating WN-2 wave activities in the core region. This region appears to be dominated by WN-1 waves, which will be a subject for a future study.

Third, it may be easy to see why the height perturbation h' for the VRW peaks near the RMV and then decreases outward (Fig. 9d), based on the structure function given in Fig. 4. However, one may wonder why h' for the IGW peaks outside the RMW (Fig. 9a). This can be seen from the radial variation of the frequency (and phase speed) of the IGW, which is small near the RMW but increases gradually outward to a pure IGW frequency as determined by the basic state; that is, Eq. (15′) becomes $\hat{\omega}_G = \overline{\Omega}_0 n \pm c_0 \overline{m}$ far outward from the RMW. It is evident that the IGW is highly unbalanced, as also indicated by larger divergence, as compared to the VRW. On the other hand, the mixed VRIGW exhibits some mixed properties of the perturbation height–wind relations between the IGW and VRW.

The propagation characteristics of the three different waves are of particular interest because they all show the generation of spiral bands in both the perturbation winds and heights after an hour (see the central panel in Fig. 9); they are analogous in many aspects to spiral rainbands seen in TCs. Note that the spiral bands form as the radial widths of the height–wind perturbations shrink with time, which leads to increases in the radial WN (e.g., from WN-1 to about WN-2 at $t = 1$ h, especially for the IGW). This feature could be attributed to the fact that each portion of the radially distributed perturbations tends to propagate azimuthally at a speed (or a Doppler-shifted frequency; i.e., $\overline{\omega}$) differing from that at its neighboring radius because of the differential rotational flows of the mean vortex. This would tend to shift the wave phases radially with time, causing their radial ''propagation'' in a spiral manner. The higher the wave frequency (and the phase speed), the more the radial WN (i.e., m) would increase, which is consistent with Fig. 6. This result appears to provide an alternative explanation, besides the radial propagation of VRWs as previously hypothesized, for the generation of spiral rainbands in TCs. That is, spiral rainbands may result from the radial differential displacements of azimuthally propagating VRWs and mixed VRIGWs.

Figures 9a and 9b show that IGWs propagate azimuthally in opposite directions at speeds faster than those of the VRW, especially outside the RMW. In contrast, the VRW propagates azimuthally in opposite directions cyclonically inside and anticyclonically outside the RMV because of the sign change of β_0 (Figs. 9d,e). The mixed VRIGW propagates at speeds between the IGW and VRW and also propagates azimuthally in a direction opposite to that of the VRW with the sign change of β_0.

5. Summary and concluding remarks

In this study, a theory for three classes of allowable waves (i.e., IGWs, VRWs, and mixed VRIGWs) in TCs, as constrained by PV conservation, is developed using a rotating shallow-water equations model in which both the rotational and divergent components are retained. A cloud-resolving simulation of Hurricane Andrew (1992) is used as a basic-state TC vortex to help simplify the radial structure equation for perturbation flows, define scaling parameters, and determine the radial distribution of various important quantities. In particular, this dataset facilitates the transformation of the radial structure equation with variable coefficients into Bessel's equation with constant coefficients. After obtaining a radial eigenvalue from Bessel equation, a cubic frequency equation for azimuthally propagating (radially discrete) waves is derived with three groups of allowable wave frequencies, depending on the sign of the discriminant Q.

It is shown that when $Q > 0$, low-frequency VRWs and high-frequency IGWs will coexist in TCs, with separable dispersion characteristics. When $Q = 0$, mixed VRIGWs with inseparable dynamical properties may appear. When $Q < 0$, there will be a low-frequency propagating mixed-VRIGWs solution and two oppositely propagating mixed-VRIGWs solutions with mixed-wave instability. It is found that the criteria of $Q > 0$ and $Q \leq 0$ are often met respectively in the eye or outer regions and in the eyewall. Results show that high-frequency IGWs in the eyewall tend to propagate at half speeds whereas the eyewall region favors the development of mixed VRIGWs with possible mixed-wave instability. Shorter waves will grow at rates that are higher than longer waves. This finding appears to help explain the development of polygonal eyewalls as well as multiple vortices in intense TCs.

The perturbation structures and propagation characteristics of WN-2 waves are examined. Results shows

many similarities of the azimuthal propagation of VRWs and IGWs to those shown in the previous studies, including flow intensities, the height–wind relation, and the relative magnitudes of divergence and vorticity. By comparison, the mixed VRIGW's flows contain some mixed properties of the VRWs and IGWs and, as expected, they are both rotational and divergent at similar magnitudes. Of importance is that all the waves show the generation of spiral bands of the perturbation winds and heights as their radial widths shrink with time. We attribute this to the radial differential advection of azimuthally propagating waves due to the differential flow properties of the mean vortex, leading to the radial phase shift azimuthally. This result appears to provide an alterative explanation for the development of spiral rainbands in TCs.

Acknowledgments. We are grateful to Dr. Yubao Liu for providing the model-simulated data for Hurricane Andrew (1992) and to Profs. Dave Nolan, Mike Montgomery, Ming Zhang, and Sixun Huang as well as Dr. Chanh Q. Kieu for their critical comments on an earlier version of the manuscript. This work was supported by Natural Science Foundation of China Grant 40830958, the National Basic Research Program of China Grant 2009CB421504, U.S. NSF Grant ATM-0758609, and NASA Grant NNG05GR32G.

APPENDIX

A Derivation of the Radial Structure Equation

To make our derivation of Eq. (7) easier to follow, we may rewrite Eq. (2) in the following matrix form:

$$\begin{bmatrix} a_{11} & a_{12} & a_{13} \\ a_{21} & a_{22} & a_{23} \\ a_{31} & a_{32} & a_{33} \end{bmatrix} \begin{bmatrix} u' \\ v' \\ h' \end{bmatrix} = 0, \tag{A1}$$

and

$$\begin{bmatrix} a_{11} & a_{12} & a_{13} \\ a_{21} & a_{22} & a_{23} \\ a_{31} & a_{32} & a_{33} \end{bmatrix} = \begin{bmatrix} \left(\frac{\partial}{\partial t} + \overline{\Omega}\frac{\partial}{\partial \lambda}\right) & -\left(\overline{\eta} - r\frac{d\overline{\Omega}}{dr}\right) & \frac{g\partial}{\partial r} \\ \overline{\eta} & \left(\frac{\partial}{\partial t} + \overline{\Omega}\frac{\partial}{\partial \lambda}\right) & \frac{g\partial}{r\,\partial \lambda} \\ \left(\frac{c_0^2}{r} + c_0^2\frac{\partial}{\partial r} + \kappa g\frac{dH}{dr}\right) & \frac{c_0^2}{r}\frac{\partial}{\partial \lambda} & g\left(\frac{\partial}{\partial t} + \overline{\Omega}\frac{\partial}{\partial \lambda}\right) \end{bmatrix}. \tag{A2}$$

Clearly, care needs to be taken when the products of various operators in (A2) are calculated because some of them are not commutative, given that $\overline{\eta}$ and $\overline{\Omega}$ are function of radius r.

We first eliminate v' from (A1) by taking $a_{22} \times$ (1a) $- a_{12} \times$ (1b) and $a_{22} \times$ (1c) $- a_{32} \times$ (1b) and obtain

$$(a_{22}a_{11} - a_{12}a_{21})u' + (a_{22}a_{13} - a_{12}a_{23})h' = 0, \tag{A3a}$$

$$(a_{22}a_{31} - a_{32}a_{21})u' + (a_{22}a_{33} - a_{32}a_{23})h' = 0. \tag{A3b}$$

Then, taking $(a_{22}a_{33} - a_{32}a_{23}) \times$ (A3a) $- (a_{22}a_{13} - a_{12}a_{23}) \times$ (A3b) yields

$$\begin{aligned}&[(a_{22}a_{33} - a_{32}a_{23})(a_{22}a_{13} - a_{12}a_{23}) - (a_{22}a_{13} - a_{12}a_{23})(a_{22}a_{33} - a_{32}a_{23})]h' \\ &\quad = [(a_{22}a_{13} - a_{12}a_{23})(a_{22}a_{31} - a_{32}a_{21}) - (a_{22}a_{33} - a_{32}a_{23})(a_{22}a_{11} - a_{12}a_{21})]u'.\end{aligned} \tag{A4}$$

After some tedious manipulations and reorganization, we obtain the following high-order partial differential equation for u' and h':

$$\begin{aligned}\left[-2g\frac{d\overline{\Omega}}{dr}\left(\frac{\partial}{\partial t} + \overline{\Omega}\frac{\partial}{\partial \lambda}\right)^2\frac{\partial}{\partial \lambda} - 2g\frac{c_0^2}{r^3}\left(\frac{\partial}{\partial t} + \overline{\Omega}\frac{\partial}{\partial \lambda}\right)\frac{\partial^2}{\partial \lambda^2}\right]h' = \Bigg[&-\left(\frac{\partial}{\partial t} + \overline{\Omega}\frac{\partial}{\partial \lambda}\right)^4 + \left(\frac{\partial}{\partial t} + \overline{\Omega}\frac{\partial}{\partial \lambda}\right)^2\left(\frac{c_0^2}{r}\frac{\partial}{\partial r} - \frac{c_0^2}{r^2} + c_0^2\frac{\partial^2}{\partial r^2}\right. \\ &\left. + \kappa g\frac{dH}{dr}\frac{\partial}{\partial r} + \kappa g\frac{d^2H}{dr^2} + r\overline{\eta}\frac{d\overline{\Omega}}{dr} - \overline{\eta}^2 + \frac{c_0^2}{r}\frac{\partial^2}{\partial \lambda^2}\right) \\ &+ \left(\frac{\partial}{\partial t} + \overline{\Omega}\frac{\partial}{\partial \lambda}\right)\left(-\frac{c_0^2}{r}\frac{d\overline{\eta}}{dr}\frac{\partial}{\partial \lambda} + 2\frac{c_0^2}{r^2}\overline{\eta}\frac{\partial}{\partial \lambda} + \kappa g\frac{\overline{\eta}}{r}\frac{dH}{dr}\frac{\partial}{\partial \lambda}\right)\Bigg]u'.\end{aligned} \tag{A5}$$

Assuming the harmonic form of wave solution,

$$u' = \tilde{u}(r)\exp[i(n\lambda - \hat{\omega}t)] + \text{c.c.} \quad \text{and}$$
$$h' = \tilde{h}(r)\exp[i(n\lambda - \hat{\omega}t)] + \text{c.c.}, \tag{A6}$$

where $\tilde{u} = \tilde{u}_r + i\tilde{u}_i$ and $\tilde{h} = \tilde{h}_r + i\tilde{h}_i$. Letting $\overline{\omega} = \hat{\omega} - \overline{\Omega}n \neq 0$, where $\overline{\omega} = \overline{\omega}_r + i\overline{\omega}_i$, and substituting (A6) into (A5) gives

$$2\frac{d\overline{\Omega}}{dr}gn\overline{\omega}\tilde{h} - 2n^2g\frac{c_0^2}{r^3}\tilde{h} = i\overline{\omega}^3\tilde{u} + i\overline{\omega}\left(\frac{c_0^2}{r}\frac{d\tilde{u}}{dr} - \frac{c_0^2}{r^2}\tilde{u} + c_0^2\frac{d^2\tilde{u}}{dr^2} + \kappa g\frac{dH}{dr}\frac{d\tilde{u}}{dr} + \kappa g\frac{d^2H}{dr^2}\tilde{u} + r\overline{\eta}\frac{d\overline{\Omega}}{dr}\tilde{u} - \overline{\eta}^2\tilde{u} - \frac{c_0^2}{r^2}n^2\tilde{u}\right)$$
$$- in\tilde{u}\left(-\frac{c_0^2}{r}\frac{d\overline{\eta}}{dr} + 2\frac{c_0^2}{r^2}\overline{\eta} + \kappa g\frac{\overline{\eta}}{r}\frac{dH}{dr}\right). \tag{A7}$$

Equations (2a) and (2b) can be combined to eliminate the perturbation height in (A7); that is,

$$(\overline{\xi}\,\overline{\eta} - \overline{\omega}^2)\tilde{u} + i\left(\overline{\omega}g\frac{d\tilde{h}}{dr} - ng\overline{\xi}\frac{\tilde{h}}{r}\right) = 0,$$

where $\overline{\xi} = \partial r\overline{V}/r\,\partial r$. The scale analysis, given in section 3, shows that $d\tilde{h}/dr \ll \tilde{h}/r$ (see Fig. 1c), so the above equation can be rewritten as

$$g\tilde{h} \sim i\left(\frac{r\overline{\eta}}{n} - \frac{r\overline{\omega}^2}{n\overline{\xi}}\right)\tilde{u} = i\frac{r\overline{\eta}}{n}\left(1 - \frac{\overline{\omega}^2}{\overline{\eta}\overline{\xi}}\right)\tilde{u}.$$

Since $\overline{\xi} \sim \overline{\eta} \sim \overline{\omega} \sim 10^{-4}\text{s}^{-1}$, we have $(1 - \overline{\omega}^2/\overline{\eta}\overline{\xi}) \sim 10^{-1}$. So the two terms on the lhs of (A7) become $2i(d\overline{\Omega}/dr)r\overline{\omega}\,\overline{\eta}[1 - (\overline{\omega}^2/\overline{\eta}\overline{\xi})] \ll 2i(d\overline{\Omega}/dr)r\overline{\omega}\,\overline{\eta}$ and $2in(c_0^2/r^2)\overline{\eta}[1 - (\overline{\omega}^2/\overline{\eta}\overline{\xi})]\tilde{u} \ll 2in(c_0^2/r^2)\overline{\eta}\tilde{u}$, and they can be neglected as compared to the corresponding terms on the rhs of Eq. (7). Then, we obtain

$$c_0^2\overline{\omega}\frac{d^2\tilde{u}}{dr^2} + \overline{\omega}\left(\frac{c_0^2}{r} + \kappa g\frac{dH}{dr}\right)\frac{d\tilde{u}}{dr} + \left(\overline{\omega}^3 - \frac{c_0^2}{r^2}\overline{\omega} + \kappa g\frac{d^2H}{dr^2}\overline{\omega} + r\overline{\eta}\frac{d\overline{\Omega}}{dr}\overline{\omega} - \overline{\eta}^2\overline{\omega} - \frac{c_0^2}{r^2}n^2\overline{\omega} + \frac{c_0^2}{r}n\frac{d\overline{\eta}}{dr}\right.$$
$$\left. - 2n\frac{c_0^2}{r^2}\overline{\eta} - \kappa ng\frac{\overline{\eta}}{r}\frac{dH}{dr}\right)\tilde{u} = 0. \tag{A8}$$

Rearranging (A8) will lead to the radial structure equation for $\tilde{u}$ given in Eq. (7).

REFERENCES

Bender, M. A., 1997: The effect of relative flow on the asymmetric structure in the interior of hurricanes. *J. Atmos. Sci.,* **54,** 703–724.

Chen, Y., G. Brunet, and M. K. Yau, 2003: Spiral bands in a simulated hurricane. Part II: Wave activity diagnostics. *J. Atmos. Sci.,* **60,** 1239–1256.

Daley, R., 1981: Normal model initialization. *Rev. Geophys. Space Phys.,* **19,** 450–468.

Ford, R., 1994: The instability of an axisymmetric vortex with monotonic potential vorticity in rotating shallow water. *J. Fluid Mech.,* **280,** 303–334.

Frank, W. M., and E. A. Ritchie, 1999: Effects of environmental flow upon tropical cyclone structure. *Mon. Wea. Rev.,* **127,** 2044–2061.

Gall, R., J. Tuttle, and P. Hildebrand, 1998: Small-scale spiral bands observed in Hurricanes Andrew, Hugo, and Erin. *Mon. Wea. Rev.,* **126,** 1749–1766.

Guinn, T. A., and W. H. Schubert, 1993: Hurricane spiral bands. *J. Atmos. Sci.,* **50,** 3380–3403.

Hodyss, D., and D. S. Nolan, 2008: The Rossby–inertia–buoyancy instability in baroclinic vortices. *Phys. Fluids,* **20,** 096602, doi:10.1063/1.2980354.

Hogsett, W., and D.-L. Zhang, 2009: Numerical simulation of Hurricane Bonnie (1998). Part III: Energetics. *J. Atmos. Sci.,* **66,** 2678–2696.

Holton, J. R., 2004: *An Introduction to Dynamic Meteorology*. 4th ed. Elsevier Academic, 535 pp.

Jorgensen, D. P., 1984: Mesoscale and convective-scale characteristics of mature hurricanes. Part II: Inner core structure of Hurricane Allen (1980). *J. Atmos. Sci.,* **41,** 1287–1311.

Kossin, J. P., B. D. McNoldy, and W. H. Schubert, 2002: Vortical swirls in hurricane eye clouds. *Mon. Wea. Rev.,* **130,** 3144–3149.

Liu, Y., D.-L. Zhang, and M. K. Yau, 1997: A multiscale numerical study of Hurricane Andrew (1992). Part I: Explicit simulation and verification. *Mon. Wea. Rev.,* **125,** 3073–3093.

——, ——, and ——, 1999: A multiscale numerical study of hurricane Andrew (1992). Part II: Kinematics and inner-core structures. *Mon. Wea. Rev.,* **127,** 2597–2616.

Macdonald, N. J., 1968: The evidence for the existence of Rossby-like waves in the hurricane vortex. *Tellus,* **20,** 138–150.

Matsuno, T., 1966: Quasi-geostrophic motions in the equatorial area. *J. Meteor. Soc. Japan,* **44,** 25–43.

Montgomery, M. T., and R. J. Kallenbach, 1997: A theory of vortex Rossby waves and its application to spiral bands and intensity changes in hurricanes. *Quart. J. Roy. Meteor. Soc.,* **123,** 435–465.

——, and J. Enagonio, 1998: Tropical cyclogenesis via convectively forced vortex Rossby waves in a three-dimensional quasi-geostrophic model. *J. Atmos. Sci.,* **55,** 3176–3207.

——, and J. L. Franklin, 1998: An assessment of the balance approximation in hurricanes. *J. Atmos. Sci.,* **55,** 2193–2200.

——, M. Bell, S. D. Aberson, and M. Black, 2006: Hurricane Isabel (2003): New insights into the physics of intense storms. Part I: Mean vortex structure and maximum intensity estimates. *Bull. Amer. Meteor. Soc.,* **87,** 1335–1347.

Nolan, D. S., and M. T. Montgomery, 2000: The algebraic growth of wavenumber-one disturbances in hurricane-like vortices. *J. Atmos. Sci.,* **57,** 3514–3538.

——, ——, and L. D. Grasso, 2001: The wavenumber-one instability and trochoidal motion of hurricane-like vortices. *J. Atmos. Sci.,* **58,** 3243–3270.

Schecter, D. A., and M. T. Montgomery, 2003: On the symmetrization rate of an intense geophysical vortex. *Dyn. Atmos. Oceans,* **37,** 55–87.

——, and ——, 2004: Damping and pumping of a vortex Rossby wave in a monotonic cyclone: Critical layer stirring versus inertia-buoyancy wave emission. *Phys. Fluids,* **16,** 1334–1348.

——, and ——, 2007: Waves in a cloudy vortex. *J. Atmos. Sci.,* **64,** 314–337.

Schubert, W. H., M. T. Montgomery, R. K. Taft, T. A. Guinn, S. R. Fulton, J. P. Kossin, and J. P. Edwards, 1999: Polygonal eyewalls, asymmetric eye contraction, and potential vorticity mixing in hurricanes. *J. Atmos. Sci.,* **56,** 1197–1223.

Shapiro, L. J., and M. T. Montgomery, 1993: A three-dimensional balance theory for rapidly rotating vortices. *J. Atmos. Sci.,* **50,** 3322–3335.

Tuleya, R. E., and Y. Kurihara, 1981: A numerical study on the effects of environmental flow on tropical storm genesis. *Mon. Wea. Rev.,* **109,** 2487–2506.

Wang, X., and D.-L. Zhang, 2003: Potential vorticity diagnosis of a simulated hurricane. Part I: Formulation and quasi-balanced flow. *J. Atmos. Sci.,* **60,** 1593–1607.

Wang, Y., 2002: Vortex Rossby waves in a numerically simulated tropical cyclone. Part I: Overall structure, potential vorticity, and kinetic energy budgets. *J. Atmos. Sci.,* **59,** 1213–1238.

Willoughby, H. E., 1978: A possible mechanism for the formation of hurricane rainbands. *J. Atmos. Sci.,* **35,** 838–848.

Xu, Q., 1983: Unstable spiral inertial gravity waves in typhoons. *Sci. Sin.,* **26,** 70–80.

Yau, M. K., Y. Liu, D.-L. Zhang, and Y. Chen, 2004: A multiscale numerical study of Hurricane Andrew (1992). Part VI: Small-scale inner-core structures and wind streaks. *Mon. Wea. Rev.,* **132,** 1410–1433.

Zwillinger, D., 2003: *Standard Mathematical Tables and Formulae*. CRC Press, 910 pp.